PLOS | ONE

RESEARCH ARTICLE

Multichannel Compressive Sensing MRI Using Noiselet Encoding

Kamlesh Pawar[1,2,3], **Gary Egan**[4], **Jingxin Zhang**[1,5]*

1 Department of Electrical and Computer System Engineering, Monash University, Melbourne, Australia, **2** Indian Institute of Technology Bombay, Mumbai, India, **3** IITB Monash Research Academy, Mumbai, India, **4** Monash Biomedical Imaging, Monash University, Melbourne, Australia, **5** School of Software and Electrical Engineering, Swinburne University of Technology, Melbourne, Australia

* jingxinzhang@swin.edu.au

Abstract

The incoherence between measurement and sparsifying transform matrices and the restricted isometry property (RIP) of measurement matrix are two of the key factors in determining the performance of compressive sensing (CS). In CS-MRI, the randomly under-sampled Fourier matrix is used as the measurement matrix and the wavelet transform is usually used as sparsifying transform matrix. However, the incoherence between the randomly under-sampled Fourier matrix and the wavelet matrix is not optimal, which can deteriorate the performance of CS-MRI. Using the mathematical result that noiselets are maximally incoherent with wavelets, this paper introduces the noiselet unitary bases as the measurement matrix to improve the incoherence and RIP in CS-MRI. Based on an empirical RIP analysis that compares the multichannel noiselet and multichannel Fourier measurement matrices in CS-MRI, we propose a multichannel compressive sensing (MCS) framework to take the advantage of multichannel data acquisition used in MRI scanners. Simulations are presented in the MCS framework to compare the performance of noiselet encoding reconstructions and Fourier encoding reconstructions at different acceleration factors. The comparisons indicate that multichannel noiselet measurement matrix has better RIP than that of its Fourier counterpart, and that noiselet encoded MCS-MRI outperforms Fourier encoded MCS-MRI in preserving image resolution and can achieve higher acceleration factors. To demonstrate the feasibility of the proposed noiselet encoding scheme, a pulse sequences with tailored spatially selective RF excitation pulses was designed and implemented on a 3T scanner to acquire the data in the noiselet domain from a phantom and a human brain. The results indicate that noislet encoding preserves image resolution better than Fouirer encoding.

Citation: Pawar K, Egan G, Zhang J (2015) Multichannel Compressive Sensing MRI Using Noiselet Encoding. PLoS ONE 10(5): e0126386. doi:10.1371/journal.pone.0126386

Academic Editor: Christophe Lenglet, University of Minnesota, UNITED STATES

Received: August 15, 2014

Accepted: April 1, 2015

Published: May 12, 2015

Data Availability Statement: All relevant data are within the paper and its Supporting Information files.

Funding: The authors have no support or funding to report.

Competing Interests: The authors have declared that no competing interests exist.

1 Introduction

Magnetic resonance imaging (MRI) is a widely used imaging modality in clinical practice due to its ability to produce a good contrast between soft tissues and to image a slice at any orientation. The MRI scanner acquires data in a Fourier domain called k-space. MRI captures an

image by scanning through the k-space on a Cartesian or non-Cartesian trajectory. This scanning process is time consuming and results in a long acquisition time and patient discomfort. Accelerating the data acquisition process is an active area of research in MRI, and Compressive Sensing (CS) is a promising solution that can improve the speed of data acquisition in MRI. CS [1–5] is a technique that permits the faithful reconstruction of the signal of interest from the data acquired below the Nyquist sampling rate. MRI is a ideal system [6] for CS applications as it acquires image already in encoded form rather than in pixel domain. The application of CS in MRI was first described in [7], where variable density random under-sampling of phase encodes was suggested as a sampling strategy. Parallel imaging techniques [8–10] have also been combined with CS in [11–16] to further accelerate MRI scans, and CS-MRI has been applied for dynamic imaging, exploiting k-t space sparsity [14, 17–20].

The theory of CS provides a solution to an ill-posed inverse problem by exploiting prior knowledge of signal sparsity or compressibility. This theory guarantees perfect reconstruction of the signal from the under-sampled data if certain conditions are satisfied [1–5, 21]: (i) sparsity or compressibility of the signal in the transform domain; (ii) Restricted Isometry Property (RIP) of the measurement matrix or incoherence between the measurement and sparsifying transform matrices; and (iii) a non-linear reconstruction algorithm that promotes sparse representation of the image and enforces data consistency of reconstruction with the acquired data.

The sparsity or compressibility condition is satisfied by MR images as they are known to be sparse or compressible in the wavelet domain and the finite difference domain [7, 11–13]. However, the RIP is difficult to verify for a given deterministic measurement matrix since it is computationally NP hard [22]. An empirical solution to this problem in the CS literature is to use random measurement matrices. A randomly sampled frequency domain data can capture pertinent information from a sparse signal with fewer measurements and allows accurate reconstruction of the signal by the convex l_1 optimization program. This property was first proved mathematically for Gaussian matrices [5, 23] and has recently been extended to a wide class of random matrices [24]. Based on this property, [25] proposed using spatially selective RF pulses to implement random encoding along the phase encode direction, with the entries of the random measurement matrix drawn from Gaussian distribution. This random encoding scheme attempts to approximate the sufficient conditions for perfect CS reconstruction, but as described in [25], this measurement matrix is not unitary and results in noise amplification even after taking all the required measurements. Another problem with random encoding is computational complexity. Dense random matrices consume large amounts of memory and require computationally expensive matrix multiplications in CS-reconstruction [3, 26]. This problem is partially alleviated in [25] by using fast Fourier transforms of the matrix multiplications, but still requires more memory and computations than those of structured/unitary measurement matrices.

MRI uses the Fourier basis to encode the excited region of interest. The Fourier measurement matrix is weakly incoherent with the wavelet sparsifying transform matrix, thus is sub-optimal for CS-MRI [27]. The incoherence is essentially a measure of the spread of sparse signal energy in the measurement domain [3]. Various attempts have been made in [25, 27–30] to spread the energy of the MR signal in the measurement domain. In [27, 31], the spread spectrum technique was presented which convolves the k-space with the Fourier transform of a chirp function to spread the energy of the MR signal in the measurement domain. The chirp modulation is implemented through the use of second order shim coils. In [28–30, 32–34], other non-Fourier encoding strategies were described for compressive sensing that aims to spread the energy of the MR signal in the measurement domain. While these encoding strategies can spread the signal energy to some extent, none of them has the theoretically proven maximal incoherence for the complete spread of the signal energy.

Noiselet bases [35, 36] are known to completely spread out the energy of the signal in the measurement domain, which is a desired property in CS. Noiselets are also known to be maximally incoherent with Haar wavelets that makes them the best suited bases for CS. Further, noiselet matrices are complex valued, symmetric and unitary, which simplifies the implementation of image reconstruction program in CS-MRI. In the simulation study of [37], it is found that the noiselet measurement matrix outperforms the chirp modulation measurement matrix when the noise level is high. Also, as shown in Section III of this paper, the multichannel noiselet measurement matrix exhibits much better RIP than that of its Fourier counterpart. In order to take the advantage of maximal incoherence and better RIP provided by noiselet measurement matrix, we have investigated the use of noiselet encoding for CS-MRI.

In order to take the advantage of multiple measurements provided by an MR scanner through the use of multiple channels, a Multichannel Compressive Sensing (MCS) framework is proposed in [11] for CS reconstructions. The MCS framework simultaneously uses data from the multiple channels to reconstruct the desired image instead of reconstructing separate images from each channel, resulting in higher acceleration factors and improved image quality. Therefore, in this paper we describe the theory and implementation details of using noiselet bases as the measurement matrix in MCS-MRI. Considering the lack of analysis and sufficient understanding of MCS-MRI in the literature, we also present an empirical RIP analysis of the multichannel noiselet measurement matrix in comparison with its Fourier counterpart. The simulation and experimental results indicate that the multichannel noiselet measurement matrix outperforms its Fourier counterpart, and that noiselet encoding outperforms Fourier encoding in preserving image resolution for the same acceleration factors, and can achieve higher acceleration factors than the Fourier encoding scheme for the desired image quality and resolution.

The paper is organized as follows. In section 2, we describe the background of CS, sufficient conditions for CS and develops a model for MCS-MRI reconstruction. The noiselet basis function, its properties and our motivation for using noiselets in MRI is presented here. In section 3, a pulse sequence design to implement the proposed noiselet encoding scheme is described, followed by an empirical RIP analysis of the multichannel noiselet measurement matrix in comparison with its Fourier counterpart. In section 4, simulation studies comparing the performance of noiselet encoded and Fourier encoded MCS-MRI for different acceleration factors are demonstrated on a brain image. The effect of the number of channels and level of noise on the reconstruction is also evaluated for both the encoding schemes. We demonstrate the feasibility of the proposed encoding scheme by acquiring noiselet encoded data from a phantom and a human brain. In section 5, we discuss the findings, limitation and further extension of the technique and section 6 concludes the contribution of this work.

2 Theory

2.1 Compressive Sensing

Compressive sensing is a mathematical theory describing how a sparse signals can be faithfully recovered after sampling its projections well below the Nyquist sampling rate. Consider a signal x in the n dimensional complex space $\mathbb{C}^n$ that can be sparsely represented in Ψ domain as $\rho = \Psi x$, where Ψ is the $n \times n$ sparsifying transform matrix satisfying $\Phi^*\Phi = I$. The signal ρ is K-sparse, that is, only the K coefficients in ρ are non-zero. A measurement system measures signal y in m dimensional space by taking only m projections of the signal x as

$$y = \Phi x \tag{1}$$

In CS MRI, $x \in \mathbb{C}^n$ is the vectorized image with the dimension $n = pq$ for a $p \times q$ image, and $\Phi \in \mathbb{C}^{m \times n}$ is usually a (partially) randomly under-sampled discrete Fourier transform matrix resulting from encoding process, where $m = rq$ and $r < p$ is the number of phase encoding lines used to acquire y. Given the image size $p \times q$, the under-sampling ratio $n/m = p/r$ is determined by the number of phase encoding lines, r, used in data acquisition, which in turn determines the reduction of data acquisition time [7]. So the under-sampling ratio $n/m = p/r$ is called the acceleration factor in CS MRI.

Eq (1) can be further expressed as

$$y = \Phi\Psi^*\rho, \quad x = \Psi^*\rho \tag{2}$$

where * represents the conjugate transpose operation and the signal x is sparse in the Ψ domain. MR images can be sparsely represented in the wavelet domain using the wavelet transform matrix. Given the measurement y and the matrices Φ and Ψ, there exist many solutions satisfying (1) and recovering x becomes an ill posed problem. The CS theory provides a unique solution to the ill-posed problem by solving the following optimization program:

$$\min_{\hat{x}} \quad \|\Psi\hat{x}\|_{l_1} \qquad s.\,t. \qquad y = \Phi\hat{x} \tag{3}$$

where $\|x\|_{l_1} := \Sigma_i |x_i|$ is the l_1 norm of x, with x_i the ith element of x. Exact reconstruction of the signal x is achievable if certain mathematical conditions hold.

2.2 Restricted Isometry and Incoherence in Compressive Sensing

An important sufficient condition for exact reconstruction of x is the so called restricted isometry property (RIP) [2, 21, 23]. For a normalized measurement matrix Φ with unit column norms, the RIP is given as

$$(1 - \delta_K)\|x\|_{l_2}^2 \leq \|\Phi x\|_{l_2}^2 \leq (1 + \delta_K)\|x\|_{l_2}^2 \tag{4}$$

where $\delta_K \in (0,1)$ is called the RIP constant. The RIP (4) is equivalent to [2, 38, 39]

$$(1 - \delta_K) \leq \sigma_{min}^2[\Phi_{sub}(K)] \leq \sigma_{max}^2[\Phi_{sub}(K)] \leq (1 + \delta_K), \tag{5}$$

where $\Phi_{sub}(K)$ is the $m \times K$ submatrix formed from K distinct columns of Φ, and $\sigma_{min}[\Phi_{sub}(K)]$ and $\sigma_{max}[\Phi_{sub}(K)]$ are the minimum and maximum singular values of $\Phi_{sub}(K)$, respectively (In [2, 38, 39], the eigenvalue $\lambda[\Phi_{sub}(K)^*\Phi_{sub}(K)]$ is used for (5), where $\lambda[\Phi_{sub}(K)^*\Phi_{sub}(K)] = \sigma^2[\Phi_{sub}(K)]$). The RIP constant δ_K is the smallest constant that satisfies the inequality (5) for every $m \times K$ sized submatrix of Φ, and it is essentially a bound on the distance between unity and the singular values of all $\Phi_{sub}(K)$s. It is shown in [23] that if $\delta_{2K} < 1$, then a K-sparse signal x can be exactly reconstructed from the measurements of Φ.

While $\delta_K \in (0,1)$ renders the exact reconstruction of x, the value of δ_K determines the stability of reconstruction. In the presence of measurement noise ϵ, $y = \Phi x + \epsilon$ and the reconstructed signal $\hat{x}$ satisfies (Section 5.2 in [40])

$$\|x - \hat{x}\|_{l_2}^2 \leq \frac{4\epsilon^2}{1 - \delta_{2K}}. \tag{6}$$

Thus, the smaller the δ_K, the smaller the reconstruction error, and vice versa. Since measurement noise always exists in practice, the value of δ_K is an important performance measure of a measurement matrix Φ for both the reconstruct-ability and reconstruction error. However, the computation of δ_K for a given Φ is NP hard and hence intractable. Since the RIP constant δ_K is essentially a bound on the distance between 1 and the singular values of all $\Phi_{sub}(K)$s, the value

of δ_K can be assessed by the distances from 1 to the $\sigma_{min}[\Phi_{sub}(K)]$s and $\sigma_{max}[\Phi_{sub}(K)]$s. The smaller the distance, the smaller the δ_K and hence the better performance of Φ. Since (5) must hold for all the $m \times K$ submatrices of Φ, the statistics of $\sigma_{min}[\Phi_{sub}(K)]$ and $\sigma_{max}[\Phi_{sub}(K)]$ over randomly sampled $\Phi_{sub}(K)$s are used in [5, 38, 39] to assess the RIP performance of a given measurement matrix Φ. This method is also adopted in this paper.

Another important sufficient condition for exact reconstruction of x is the incoherence [3, 36]. For a pair of measurement matrix Φ and sparsifying transform matrix Ψ, satisfying $\Phi^*\Phi = nI$ and $\Psi^*\Psi = I$, their incoherence is defined as

$$\mu(\Phi, \Psi) = \max_{k,j} |\langle \Phi_k, \Psi_j \rangle| \tag{7}$$

where Φ_k and Ψ_j are respectively the k^{th} and j^{th} columns of Φ and Ψ, and $\mu(\Phi, \Psi) \in [1, \sqrt{n}]$. The value $\mu(\Phi, \Psi) = 1$ is termed as maximal incoherence. As shown in [3], if $m \geq C \cdot \mu^2(\Phi, \Psi) \cdot K \cdot log(n)$, where C is a small constant, then a K-sparse signal x can be exactly reconstructed. Thus, $\mu(\Phi, \Psi)$ determines the minimum number of measurements needed for exact reconstruction of x. The smaller the $\mu(\Phi, \Psi)$, the smaller the m (the fewer the measurements) needed for exact reconstruction of x.

It is important to note that both the RIP and the incoherence are sufficient conditions on the measurement matrix. So they are parallel and either or both of them can be used to design, analyze and assess the measurement matrix for exact reconstruction of x.

2.3 Multichannel Compressive Sensing

MRI systems acquire multiple measurements of the desired signal through multiple channels. Given the multiple channels, the data acquisition process can be modeled as $y_i = \Phi\Gamma_i x = \Phi\Gamma_i\Psi^*\rho$, $i = 1, 2, \cdots, L$, where $\Gamma_i = diag[\gamma_{ij}]_{j=1,2,\cdots,n}$ is the complex valued sensitivity map matrix of the ith receive channel, with γ_{ij} being the sensitivity of the ith channel at the jth pixel of the vectorized image, L is the number of receive channels, y_i is the data acquired from the ith receive coil and $\rho = \Psi x$. In matrix form, the y_is can be written as

$$Y := \begin{bmatrix} y_1 \\ y_2 \\ \vdots \\ y_L \end{bmatrix} = \begin{bmatrix} \Phi\Gamma_1 \\ \Phi\Gamma_2 \\ \vdots \\ \Phi\Gamma_L \end{bmatrix} x =: Ex = E\Psi^*\rho. \tag{8}$$

As seen from above, with L receive channels, the measurement matrix for x becomes E, which has a column of L sub-matrices $\Phi\Gamma_i$s and dimension $Lm \times n$. These L sub-matrices, $\Phi\Gamma_i$s, share a common measurement matrix $\Phi \in \mathbb{C}^{m \times n}$ resulting from the encoding process, so they measure the same x simultaneously with the same under-sampling pattern and under-sampling ratio n/m. As discussed in Section 2.1, the under-sampling ratio n/m is solely determined by the number of phase encoding lines used in data acquisition, hence it is independent of the number of channels L. It is important to note that Γ_is are complex valued and $\Gamma_i \neq \Gamma_j$, $i \neq j$, in general. Therefore, $\Phi\Gamma_i \neq \Phi\Gamma_j$ for $i \neq j$ and can be independent of each other, depending on the specific phase values of Γ_i and Γ_j. As a result, the multichannel measurement matrix E provides more independent measurements than that of the single channel Φ, which may improve RIP. The improved RIP may in turn reduce the number of measurements, m, and hence the number of phase encoding lines needed for exact reconstruction of x. This reasoning is confirmed by the empirical RIP analysis of E in Section 3.4.

In light of the above discussion, the following MCS optimization is considered for reconstructing the desired image x from the multichannel measurements of MRI.

$$\min_{\hat{x}} \quad \|\Psi\hat{x}\|_{l_1} \quad s.t. \quad \|Y - E\hat{x}\|_{l_2} \leq \epsilon \tag{9}$$

where Ψ is the wavelet transform operator and ϵ determines the allowed noise level in the reconstructed image.

MR images are also known to be sparse in the total variation (TV) domain. It is demonstrated in [41] that the TV penalty is critical to the performance of CS-MRI, and that MR images can be recovered more efficiently with the use of TV penalty together with the wavelet penalty. Therefore, most of the CS-MRI work [6, 7, 12, 13, 25, 28, 30, 33, 34] has used both TV and wavelet penalties for better reconstruction performance. To be consistent with this common practice in CS-MRI, the TV penalty is included in the objective function (9) for MCS-MRI reconstruction, together with the wavelet penalty. Eq (9) is a constrained optimization problem which is computationally intensive to solve. To relax the problem, (9) is converted to the unconstrained optimization problem with the inclusion of TV penalty.

$$\min_{\hat{x}} \quad \lambda_1\|\Psi\hat{x}\|_{l_1} + \lambda_2\|TV\hat{x}\|_{l_1} + \|Y - E\hat{x}\|_{l_2}^2 \tag{10}$$

where TV is a 2D total variation operator and λ_1, λ_2 are regularization parameters for wavelet and TV penalties, respectively.

Daubechies-4 (db-4) wavelet is usually used in CS-MRI because of its superior performance in sparsifying the MR images. To be consistent with this fact and fair in comparison with the existing CS-MRI results, the unconstrained objective function (10) with the Ψ of the db-4 wavelet operator will be used throughout all the simulations and reconstructions in this work.

2.4 Noiselets

Noiselets are functions which are noise-like in the sense that they are totally incompressible by orthogonal wavelet packet methods [35, 36]. Noiselet basis functions are constructed similar to the wavelet basis functions, through a multi-scale iteration of the mother bases function but with a twist. As wavelets are constructed by translates and dilates of the mother wavelet function, noiselets are constructed by twisting the translates and dilates [3]. The mother bases function $\chi(x)$ can be defined as

$$\chi(x) = \begin{cases} 1 & x \in [0,1) \\ 0 & \text{otherwise} \end{cases}$$

The family of noiselet basis functions are generated in the interval [0,1) as

$$\begin{aligned} f_1(x) &= \chi(x) \\ f_{2n}(x) &= (1-i)f_n(2x) + (1+i)f_n(2x-1) \\ f_{2n+1}(x) &= (1+i)f_n(2x) + (1-i)f_n(2x-1) \end{aligned} \tag{11}$$

where $i = \sqrt{-1}$ and $f_{2^n}, \ldots\ldots, f_{2^{n+1}}$ form the unitary basis for the vector space V_n. An example

of a 4×4 noiselet transform matrix is given below.

$$\frac{1}{2}\begin{bmatrix} 0-1i & 1+0i & 1-0i & 0+1i \\ 1+0i & 0+1i & 0-1i & 1-0i \\ 1-0i & 0-1i & 0+1i & 1+0i \\ 0+1i & 1-0i & 1+0i & 0-1i \end{bmatrix} \tag{12}$$

Noiselets totally spread out the signal energy in the measurement domain and are known to be maximally incoherent with the Haar wavelet. The mutual incoherence parameter between the noiselet measurement matrix Φ and the sparsifying Haar wavelet transform matrix Ψ has been shown to be equal to 1 [3], which is the minimum value possible for the incoherence. Therefore, theoretically, noiselets are the best suited measurement basis function for CS-MRI when the wavelet is used as sparsifying transform matrix.

2.5 Motivation

The motivations behind using noiselets as a measurement matrix in MCS-MRI are as follows:

- Noiselets completely spreads out the signal energy in the measurement domain and are maximally incoherent with wavelets.
- Noiselet basis function is unitary and hence does not amplify noise as in the case of random encoding [25].
- Unlike random basis, noiselet basis has conjugate symmetry. Thus, this property of symmetry can be exploited by using the partial Fourier like technique.
- Noiselets are derived in the same way as wavelets, therefore it can be modelled as a multiscale filter-bank and can be applied in $O(n \cdot log(n))$.

We proposed to use the noiselet encoding in the phase encode (PE) direction in 2D MR imaging. Therefore, the acquired data is noiselet encoded in the PE direction and Fourier encoded in the frequency encode (FE) direction.

3 Methods

Ethics statement: Written ethics approval was taken from Monash University Human Research Ethics Committee (MUHREC), project approval CF12/1908—2012001051 for all the human experiments performed in this study and written consent was taken from all the volunteers for *invivo* scans.

3.1 Pulse Sequence Design for Noiselet Encoding

In conventional 2D MR imaging sequences, a spatially selective RF excitation pulse is used to select the slice and the linear spatial gradients are used to encode the excited slice onto the Fourier transform space. In [31, 32, 42, 43], it is demonstrated that the spatially selective RF excitation pulse can also be used to encode the imaging volume. In [25, 32, 44, 45], the wavelet, SVD and random encoding profiles have been implemented using the spatially selective RF excitation pulses. An analysis using the linear response model described in [42] provides a theoretical framework to design spatially selective RF excitation pulses for implementation of non-Fourier encoding. Under the small flip angle ($\leq 30°$) regime, the RF pulse envelope can be calculated

directly by taking the Fourier transform of the desired excitation profile. However this method of designing an RF excitation pulse requires excellent RF and main field homogeneity.

To excite a noiselet profile during excitation, one can design an RF pulse envelope by directly taking the Fourier transform of the noiselet basis functions. For an image of size 256 × 256, the noiselet measurement matrix has 256 rows and 256 columns (refer to (12) for the low dimensional example). The Fourier transform of each row of the noiselet matrix will result in 256 RF pulse envelops. To achieve a specific flip angle, say 10 degrees, using such noiselet RF pules, the integral of each individual noiselet pulse envelope over time must equal that of the sinc RF pulse used in Fourier encoding for the same flip angle [46]. This *equal integral* rule can be used to determine the scaling of noiselet pulse envelops for a required flip angle. Compared to a sinc RF pulse of the same energy, a noiselet pulse envelope tends to have a smaller integral since its phase changes are more diverse than that of sinc pulse. Therefore, noiselet pulses generally require more energy than that of sinc RF pulse to attain the same flip angle. But the energy difference is generally marginal and hence the resulting SAR level of noiselet encoding is comparable to that of Fourier encoding. See Section 4.4 for experiment example.

A pulse sequence for the noiselet encoding of 2D MR imaging is shown in Fig 1. The pulse sequence is designed by tailoring the spin echo sequence. The RF excitation pulse in the conventional spin echo sequence is replaced by the noiselet RF pulse, and the slice select gradient is shifted to phase encoding axis. The 180° refocusing RF pulse is used in conjunction with the slice selection gradient to select the slice that refocuses the spins only in the desired slice. Spoilers are used after the readout gradient to remove any residual signal in the transverse plane. A new RF excitation pulse is used for every new TR to excite a new noiselet profile, and a total of 256 TR are required for excitation of the complete set of noiselet bases. The readout gradient strength determines the FOV in the readout direction, while the phase encoding gradient strength and duration of the RF excitation pulse determines the field of view (FOV) in phase

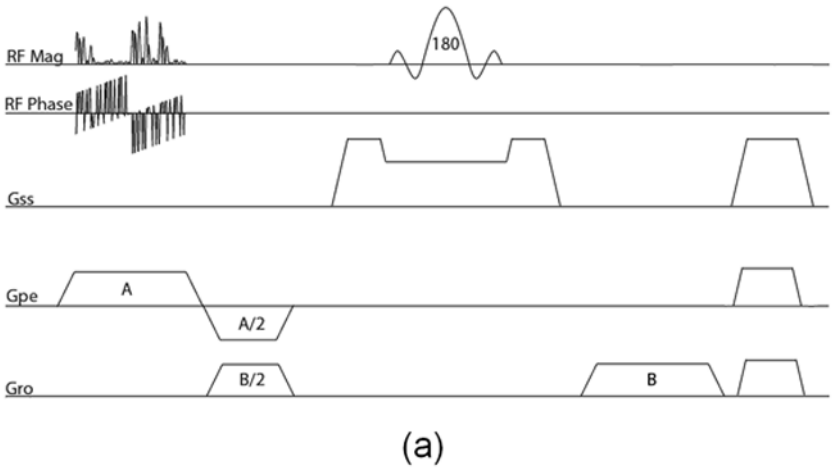

Fig 1. (a): Pulse sequence diagram for implementation of noiselet encoding in 2D imaging, where G_{ss} is the gradient in slice (z) direction, G_{pe} is the gradient in phase encoding (y) direction, and G_{ro} is the gradient in readout (x) direction. The RF flip angle is 10°, which excites a noiselet profile along y-direction. The 180° refocusing pulse is used to select the desired slice in z-direction. A new RF pulse is executed for every new TR and the complete acquisition of all noiselet basis functions requires 256 different RF pulses derived from the noiselet measurement matrix.

doi:10.1371/journal.pone.0126386.g001

encoding direction. The FOV in phase encoding direction is determined as

$$FOV_{pe} = \frac{1}{\gamma G_y \Delta t_p} \tag{13}$$

where G_y is the gradient strength in PE direction, γ is the gyromagnetic ratio, and Δt_p is the dwell time of the RF pulse which is defined as Δt_p = (Duration of RF pulse) / (Number of points in RF pulse). Eq (13) is used to calculate the gradient strength G_y required in the phase encoding direction during execution of RF excitation pulse.

3.2 Under-sampling in noiselet encoding

Noiselet transform is a type of Haar-Walsh transform. The noiselet transform coefficients totally spread out the signal in scale and time (or spatial location) [35]. As a result, each subset of the transform coefficients contains a certain information of the original signal at all the scales and times (spatial locations), and can be used alone with zero padding to reconstruct the original signal at a lower resolution. This important property is demonstrated by the example shown in Fig 2.

Fig 2 shows a brain image of size 256 × 256, and the 3D magnitude map of the noiselet transform of the brain image along the phase encoding direction (all noiselet encodes). Fig 2 (c)–2(f) shows the images reconstructed with the first, second, third and fourth 64 noiselet encodes by zero padding the rest. Each of these images are reconstructed using one quarter of the noiselet encodes and has low resolution than the original image. However, each of these images have complementary information about the original image and have approximately the same

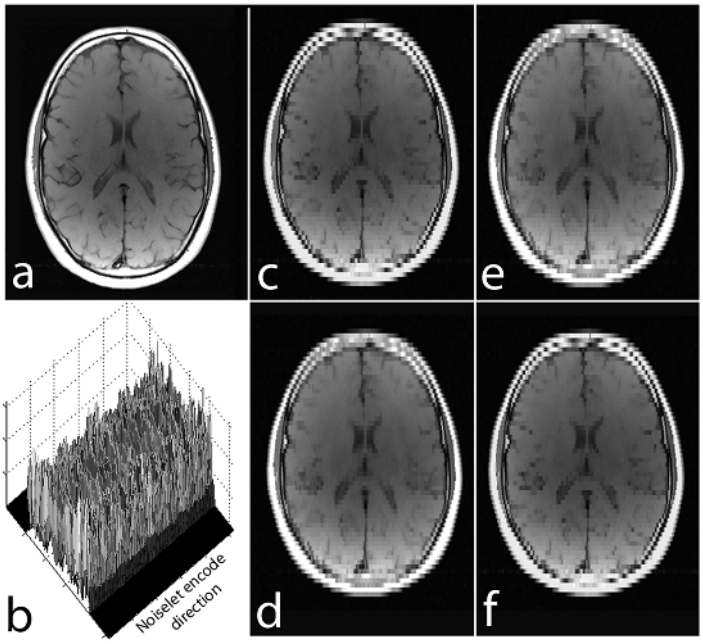

Fig 2. (a): Brain image of size 256 × 256; **(b)**: 3D magnitude map of the noiselet transform of the brain image along phase encoding direction (noiselet encodes); **(c)**: image reconstructed using only the first 64 noiselet encodes; **(d), (e) and (f)**: are the images reconstructed with the second, third and fourth 64 noiselet encodes respectively.

doi:10.1371/journal.pone.0126386.g002

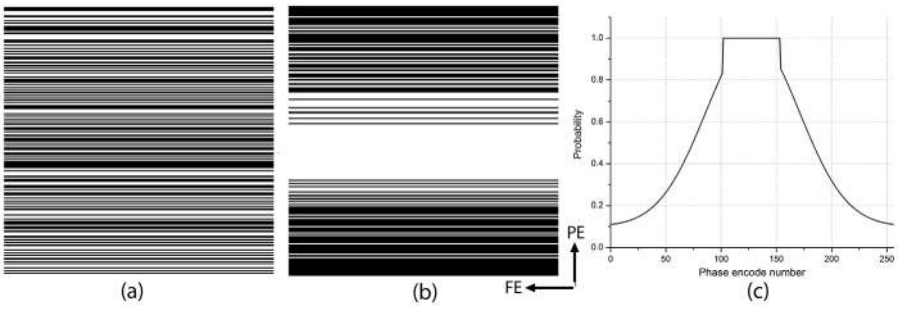

Fig 3. (a): Completely random sampling pattern for noiselet encoding generated using the uniform probability distribution function, where the white lines represent the sampled phase encodes; **(b)**: variable density random under-sampling pattern for the Fourier encoding scheme, with the sampling mask generated according to Gaussian probability distribution function; and **(c)**: probability distribution function used to generate variable density random undersampling pattern where the probability of sampling the center phase encodes is equal to 1, while the probability decays as a Guassian function with distance from the center phase encodes. The central fully sampled region is always between 20%-25% of the total number of sampled phase encodes.

doi:10.1371/journal.pone.0126386.g003

amount of energy and information because they are reconstructed using the same size of partial matrix from the original coefficient matrix.

Based on the above property of noiselet transform, we propose to under-sample the noiselet encoded data along the phase encoding direction according to the uniform probability distribution function. One sampling mask using this scheme is shown in Fig 3(a) where the white lines represent the sampled data points and the black lines represent the unsampled data points. Fig 3(b) shows the sampling mask for Fourier encoding scheme drawn from a variable density probability distribution function shown in Fig 3(c).

3.3 Coil Sensitivity Estimation

The performance of the MCS-MRI reconstruction depends on the accuracy of the sensitivity matrix estimated. We used the regularized self-calibrated estimation method [47] to estimate the sensitivity maps from the acquired data. This method estimates the sensitivity map $\hat{\Gamma}_i$ of the ith receive coil by using

$$\hat{\Gamma}_i = \min_{\Gamma} \frac{1}{2} \|I_i - \Gamma I_{ref}\|^2 + \beta R(\Gamma) \tag{14}$$

where $i \in [1, 2, \cdots, L]$ and $R(\Gamma)$ is a spatial roughness penalty function with weighting factor β. The reference image I_{ref} can be obtained using the sum of squares of individual coil images I_i's. For the experimental results presented below, the sensitivity maps were estimated from fully sampled images using (14). The data was acquired using a 32 channel head coil, but only the data from 14 channels with good SNR was used in the reconstruction.

3.4 Empirical RIP analysis of measurement matrix

According to the CS theory summarized in Section 2.2, the measurement matrix is crucial to the performance of CS reconstruction, and the performance of a measurement matrix Φ for a K-sparse signal x can be assessed by the statistics of $\sigma_{min}[\Phi_{sub}(K)]$ and $\sigma_{max}[\Phi_{sub}(K)]$ over the $\Phi_{sub}(K)$s consisting of k distinct columns of Φ. To understand the behavior and advantage of

the noiselet encoding proposed above, we have used this method to assess the noiselet measurement matrix in comparison to the conventional Fourier measurement matrix.

In the assessment, the size of the signal was $n = 256$, the number of measurements $m = 100$, the number of channels $L = 1$,8 and 14, and the sparsity K was varied from 5 to 100 with an increment of 5. For $L = 1$, the measurement matrices, Φs, were generated for the noiselet and Fourier encodings, respectively. For $L = 8$ and 14, the measurement matrices Es as given in (8) were generated for the noiselet and Fourier encodings, respectively. For each K, 2000 submatrices $\Phi_{sub}(K)$s were drawn uniformly randomly from the columns of Φ, then the $\sigma_{min}[\Phi_{sub}(K)]$ and $\sigma_{max}[\Phi_{sub}(K)]$ of every $\Phi_{sub}(K)$ were calculated. The same procedure is used to obtain the submatrices $E_{sub}(K)$s from E and to calculate the $\sigma_{min}[E_{sub}(K)]$ and $\sigma_{max}[E_{sub}(K)]$ of every $E_{sub}(K)$. The statistics of $\sigma_{min}[\Phi_{sub}(K)]$s, $\sigma_{max}[\Phi_{sub}(K)]$s, $\sigma_{min}[E_{sub}(K)]$s and $\sigma_{max}[E_{sub}(K)]$s were accumulated from their respective 2,000 samples.

Fig 4 shows the means and standard deviations of the minimum and maximum singular values of $\Phi_{sub}(K)$s and $E_{sub}(K)$s versus the sparsity K for the Fourier and noiselet measurement matrices. As seen from the figure, in single channel case, the singular values of noiselet measurement matrix are closer to 1 than those of Fourier measurement matrix, but are not significantly different. As the number of channels increases, the singular values of noiselet and Fourier measurement matrices all move towards 1, but those of noiselet measurement matrix move much closer to 1 than those of Fourier measurement matrix. By the CS theory, when the maximum distance from unity to the singular values is less than 1, it equals roughly the RIP constant δ_K. Therefore, the figure actually reveals two facts: 1) For both the noiselet and Fourier

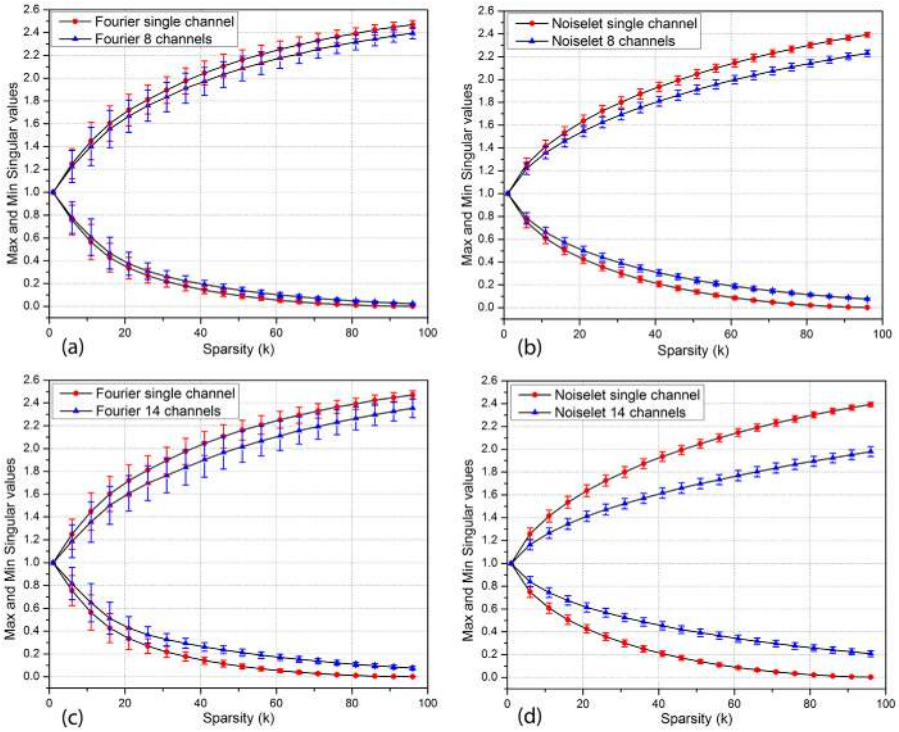

Fig 4. The means and standard deviations of maximum and minimum singular values versus sparsity K for **(a)** and **(c)**: Fourier measurement matrix, **(b)** and **(d)**: noiselet measurement matrix.

doi:10.1371/journal.pone.0126386.g004

measurement matrices, the RIP constant δ_K decreases as the number of channels increases. 2) As the number of channels increases, the RIP constant δ_K of noiselet measurement matrix deceases much more than that of Fourier measurement matrix. According to the CS theory, these imply that the multichannel measurement matrix should generally outperform the single channel measurement matrix, and that the multichannel noiselet measurement matrix should generally outperform the multichannel Fourier measurement matrix.

As a particular example consider the curves in Fig 4(d) for the noiselet measurement matrix. To facilitate discussion, the distances from unity to the singular values of a measurement matrix will be called the δ-distances here. In single channel case, the δ-distances of noiselet measurement matrix are less than 1 for $K \leq 40$. By RIP, this implies that the single channel noiselet measurement matrix can guarantee the recovery of the signals with sparsity $K \leq 20$. When the number of channels is increased to 14, the δ-distances are less than 1 for $K \leq 85$. So the 14 channel noiselet measurement matrix can guarantee the recovery of the signals with sparsity $K \leq 42$. The improvement in terms of sparsity is two folds. In contrast, for the 14 channel Fourier measurement matrix shown in Fig 4(c), its δ-distances are less than 1 only for $K < 30$, so it can only guarantee the recovery of the signals with sparsity $K < 15$.

From the above assessment, it can be expected that the multichannel CS MRI will outperform the single channel CS MRI and that the noiselet encoding multichannel CS MRI will outperform the Fourier encoding multichannel CS MRI in practice. These are confirmed by the simulation and experiment results presented in the next sections.

4 Results

4.1 Simulations

Simulations were performed on a (256 × 256) brain image acquired using a spin echo sequence to investigate the performance of noiselet encoded and Fourier encoded MRI. The simulation study was divided into two parts: (i) a simulation study with a single channel using uniform sensitivity and (ii) a simulation study with multiple channels where the sensitivity profiles were estimated from the acquired data.

4.2 Single Channel Simulation with a Uniform Sensitivity Profile

Fourier encoded CS-MRI A Fourier transform of the image was taken in the PE direction to simulate Fourier encoding. A variable density random sampling pattern as shown in Fig 3(a) where samples were taken in the PE direction according to a Gaussian distribution function was used in this simulation. A non-linear program of (10) was solved to reconstruct the final image for acceleration factors of 2 and 3. In this case the encoding matrix E does not have any sensitivity information (i.e. $E = \Phi$).

Noiselet encoded CS-MRI A noiselet transform of the image was taken in the PE direction to simulate noiselet encoding. A completely random sampling pattern was used to sample the noiselet encoded data in the PE direction and the non-linear program of (10) was solved to reconstruct the final image for acceleration factors of 2 and 3. In this case the encoding matrix E does not have any sensitivity information (i.e. $E = \Phi$).

Fig 5 show the images reconstructed with Fourier encoding and noiselet encoding using variable density random under-sampling and completely random under-sampling pattern respectively. The noiselet encoded CS-MRI performs similar to that of the Fourier encoded CS-MRI. This is due to the fact that in the case of variable density random under-sampling, the Fourier encoding judiciously exploits extra information about the data, namely the structure of k-space. The center of the k-space data has maximum energy and hence, by densely sampling the

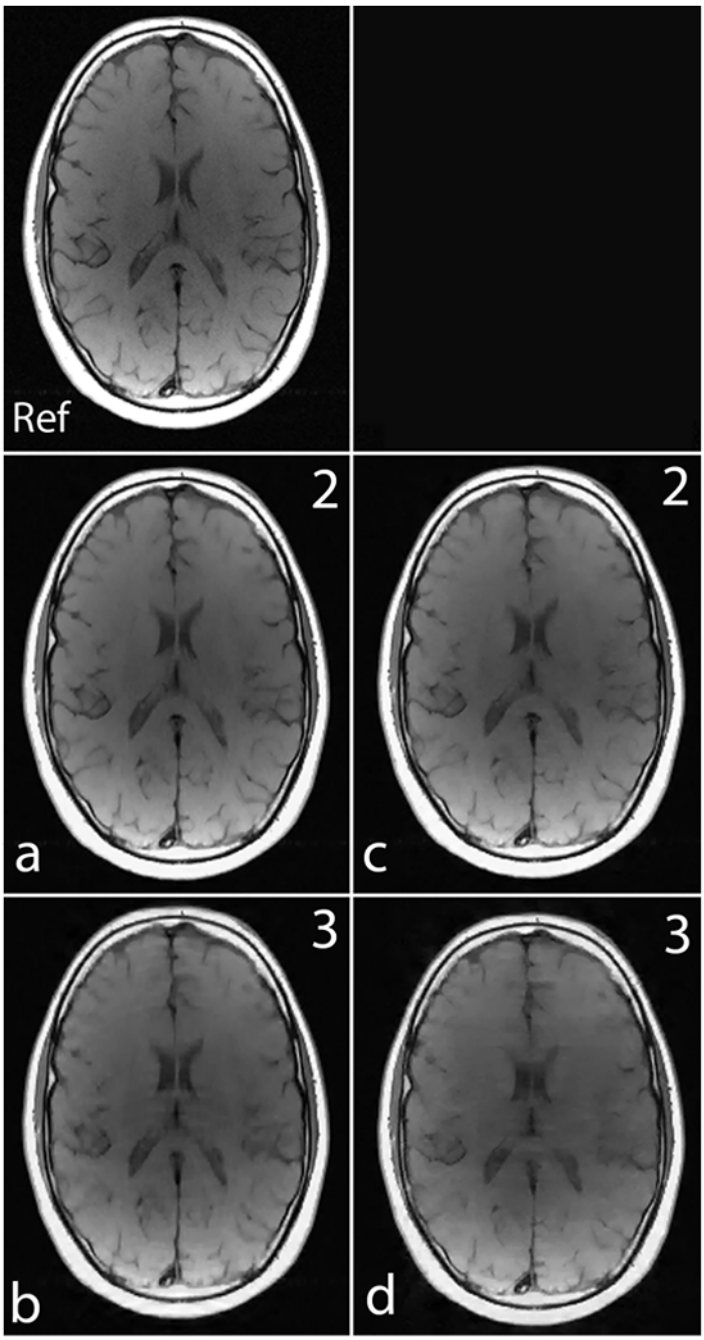

Fig 5. Ref: represents the reference image 256 × 256 (up/down: phase encodes, left/right: frequency encode); **(a)-(b)**: show images reconstructed using Fourier encoding with variable density random under-sampling patterns for acceleration factors of 2 and 3 respectively; **(c)-(d)**: show images reconstructed using noiselet encoding with completely random under-sampling patterns for acceleration factors of 2 and 3 respectively. Noiselet encoded CS-MRI performs better than the Fourier encoded CS-MRI when completely random under-sampling is used for both the encoding schemes. This is due to the better incoherence provided by the noiselets. However, noiselet encoding with a random under-sampling pattern performs similar to Fourier encoding with a variable density random under-sampling pattern.

doi:10.1371/journal.pone.0126386.g005

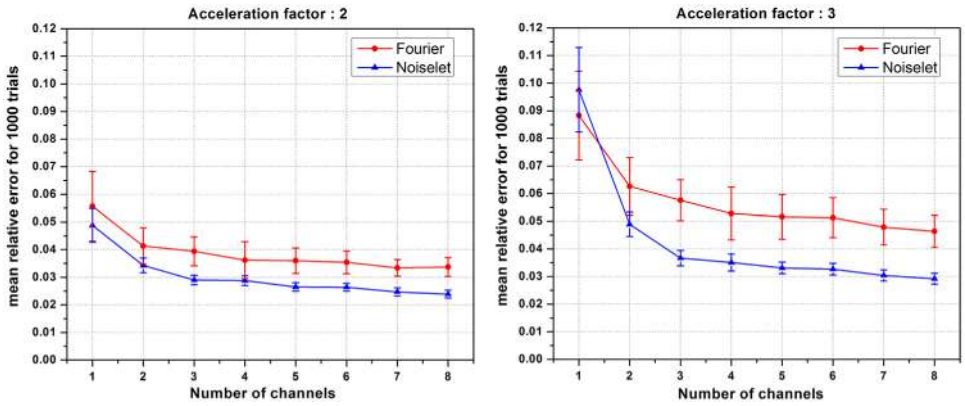

Fig 6. The mean relative error and standard deviation (vertical bar) versus the number of receive channels for acceleration factors of 2 and 3, showing that the error increases as the number of channels decreases. Noiselet encoding outperforms Fourier encoding for both acceleration factors when the number of channels is more than two. However for a single channel, noiselet encoding outperforms Fourier encoding only for the acceleration factor of 2.

doi:10.1371/journal.pone.0126386.g006

center of k-space, the Fourier encoding captures most of the signal energy and results in better performance.

In practice, the MR data is collected through the use of multiple channels, and data in each channel is slightly different from the other channels. The actual k-space data is convolved with the Fourier transform of the sensitivity profiles of the individual channel, making the data from each channel different from others. This sensitivity information can also be taken into consideration while performing the CS reconstruction, by applying the multichannel CS frame. Therefore, to further study the effect of sensitivity information on noiselet encoding and Fourier encoding, MCS-MRI simulations were performed. To quantitatively compare the performance of both the encoding schemes, we used the relative error defined in (15) as a metric:

$$Relative\ error = \frac{\|x_0 - \hat{x}\|_{l_2}}{\|x_0\|_{l_2}} \tag{15}$$

First we investigated the effect of the number of channels on the reconstruction quality using the MCS framework. For a fixed number of measurements, the number of channels was varied and the mean of the relative error for 1000 such simulations was calculated. Fig 6 shows the plot of the mean relative error versus the number of channels for the acceleration factors of 2 and 3. When the number of channels was two, the noiselet encoding scheme outperformed the Fourier encoding scheme for both the acceleration factors of 2 and 3. However, when number of channels was equal to one, the noiselet encoding outperformed the Fourier encoding for an acceleration factor of 2, but not for an acceleration factor of 3. It is interesting to note that noiselet encoding outperformed Fourier encoding for both acceleration factors when the number of channels was greater than one. These simulations suggest that noiselet encoding should take into account the sensitivity information while performing CS, and therefore noiselet encoding is potentially a better encoding scheme for MCS-MRI. Based on the fact that noiselet encoding performs better than Fourier encoding for multi-channel data, we investigated the performance of both the encoding schemes using muti-channel data.

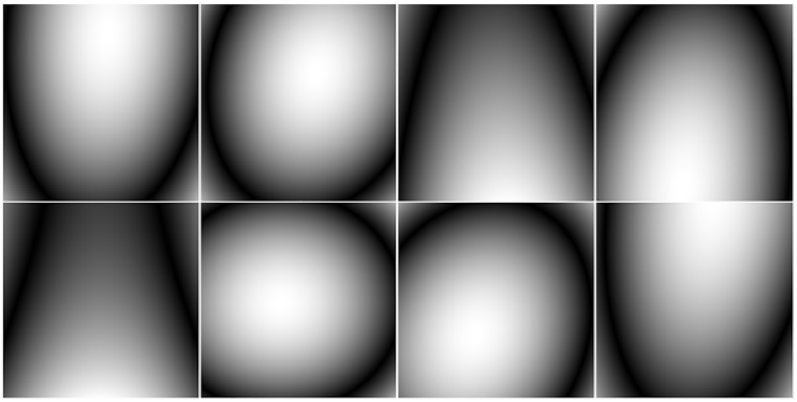

Fig 7. The eight coil sensitivity magnitude maps used in simulations that were estimated from the data acquired on MR scanner.

doi:10.1371/journal.pone.0126386.g007

4.3 Multiple Channel Simulation

A (256 × 256) brain image was used to compare the performance of noiselet encoding and Fourier encoding in MCS-MRI for different acceleration factors. Eight complex sensitivity maps (Fig 7) obtained from the head coil of a Siemens Skyra 3T scanner were used to perform the simulations. For solving the minimization program in (10), we used the nonlinear conjugate gradient with the backtracking line search method [7]. The measurement matrix (Φ) was the discrete Fourier transform matrix while the daubechies-4 wavelet transform matrix (Ψ) and TV were used as sparsifying transforms.

Fourier encoded MCS-MRI The reference brain image was multiplied by the sensitivity function to generate eight sensitivity encoded images. The Fourier transform of each these images was taken in the PE direction; only a few PEs were taken according to the Gaussian probability distribution function. MCS-MRI reconstruction of (10) was solved using the nonlinear conjugate gradient on this data. An example sampling scheme for the Fourier encoded MCS-MRI is shown in Fig 3(a).

Noiselet encoded MCS-MRI A Noiselet transform of the sensitivity encoded images was taken in the PE direction, with only a few PE selected according to the uniform probability distribution function. MCS-MRI reconstruction of (10) was solved using the nonlinear conjugate gradient on this data. An example of the sampling scheme for noiselet encoded MCS-MRI is shown in Fig 3(b).

For a noiseless simulation, the reconstructed images for different acceleration factors (4, 8 and 16) are shown in Fig 8. The difference images in Fig 8(d)–8(f) and 8(j)–8(l) demonstrate that the error in noiselet encoding is always less than in Fourier encoding, and that the noiselet encoded MCS-MRI reconstruction preserves spatial resolution better than the Fourier encoded MCS-MRI. Fig 8(m) and 8(n) show the zoomed images reconstructed with Fourier encoding for acceleration factors of 8 and 16 respectively, while Fig 8(o) and 8(p) show the zoomed images reconstructed with noiselet encoding for an acceleration factors of 8 and 16 respectively. The zoomed images highlight that the spatial resolution of the noiselet encoded reconstructions outperforms the Fourier encoded reconstructions. Moreover, the spatial resolution provided by the noiselet encoding at an acceleration factor of 16 is comparable to that of the Fourier encoding at an acceleration factor of 8, suggesting that noiselet encoding performs approximately twice as good as Fourier encoding.

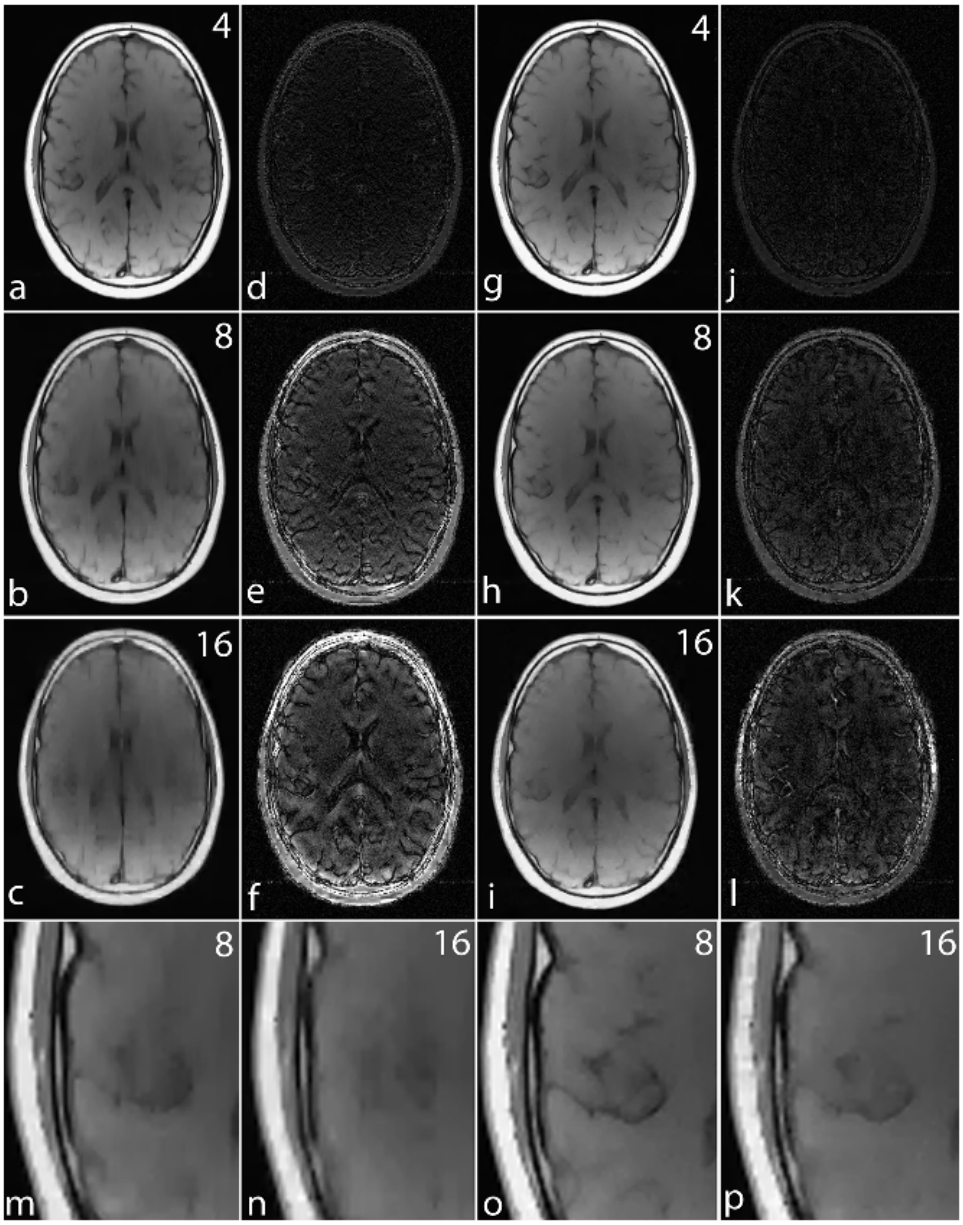

Fig 8. Simulation results for MCS-MRI comparing the noiselet encoding and Fourier encoding schemes (up/down: phase encodes, left/right: frequency encode). (a)-(c): show images reconstructed with Fourier encoding for acceleration factors of 4, 8, and 16 respectively; **(d)-(f)**: show difference images with Fourier encoding for acceleration factors of 4, 8, and 16 respectively; **(g)-(i)**: show images reconstructed with noiselet encoding for acceleration factors of 4, 8, and 16 respectively; **(j)-(l)**: show difference images with noiselet encoding for acceleration factors of 4, 8, and 16 respectively; **(m)-(n)**: show zoomed portion of images reconstructed with Fourier encoding for acceleration factors of 8, and 16 respectively; **(o)-(p)**: show zoomed portion of images reconstructed with noiselet encoding for acceleration factors of 8, and 16 respectively. The zoomed images highlight that MCS-MRI using noiselet encoding reconstructions outperforms the Fourier encoding for preserving image resolution.

doi:10.1371/journal.pone.0126386.g008

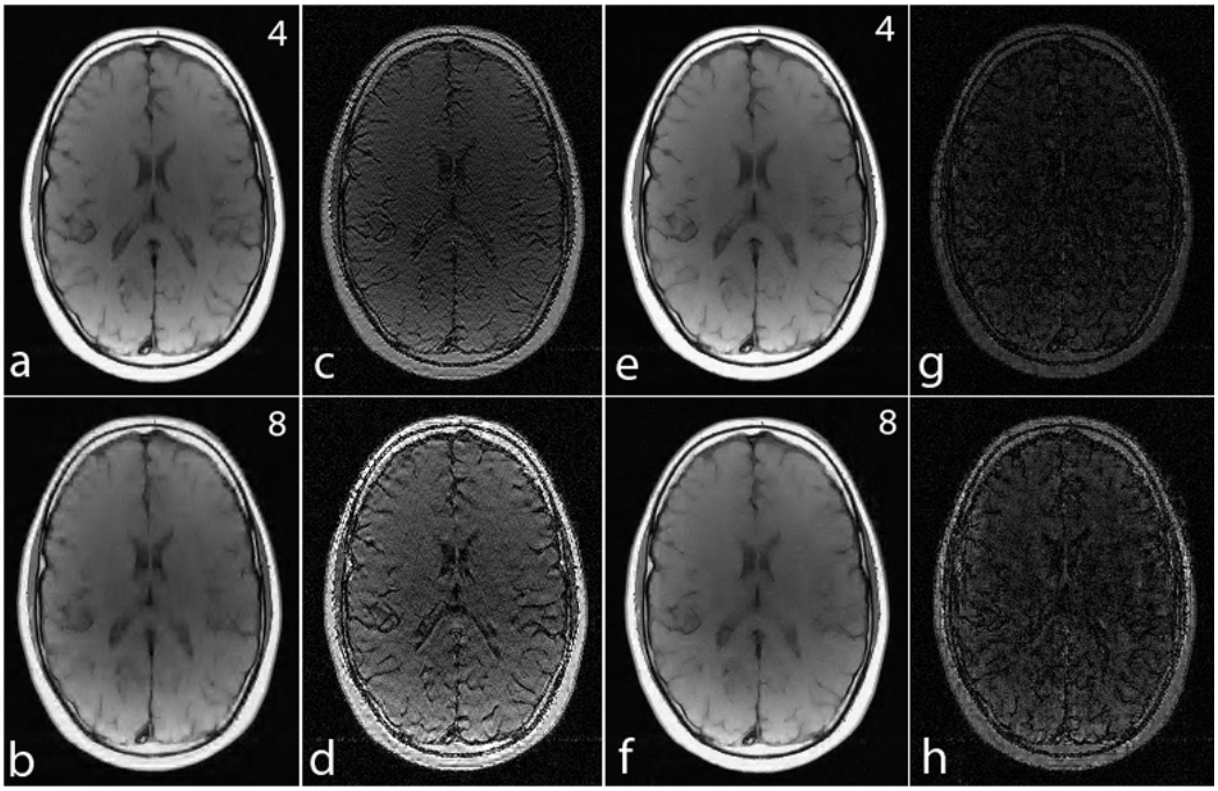

Fig 9. Simulation results for MCS-MRI comparing the noiselet encoding and Fourier encoding schemes (up/down: phase encodes, left/right: frequency encode) using only wavelet penalty. (a)-(b): show images reconstructed with Fourier encoding for acceleration factors of 4 and 8 respectively; **(c)-(d)**: show difference images with Fourier encoding for acceleration factors of 4 and 8 respectively; **(e)-(f)**: show images reconstructed with noiselet encoding for acceleration factors of 4 and 8 respectively; **(g)-(h)**: show difference images with noiselet encoding for acceleration factors of 4 and 8 respectively.

doi:10.1371/journal.pone.0126386.g009

To further compare MCS-MRI under Fourier encoding and noiselet encoding, we also reconstructed images using only the wavelet penalty in (9). As shown in Fig 9, the reconstructed images of both encoding schemes are degraded as compared to those reconstructed using both the wavelet and TV penalties. However, the superior image quality of noiselet encoding over Fourier encoding still holds true.

To measure the relative error, simulations were performed on the brain image for 1000 times by randomly generating a sampling mask each time. The mean of the relative errors was calculated after 1000 such reconstructions at every acceleration factor. The mean relative error versus the number of measurements is plotted in Fig 10 and highlights that noiselet encoding outperforms Fourier encoding for all acceleration factors. The relative error for noiselet encoding at an acceleration factor of 16 was the same as the relative error for Fourier encoding at an acceleration factor of 8 indicating that higher acceleration factors are achievable with noiselet encoding compared to Fourier encoding.

In practice, MR data always has some noise and the level of noise depends upon many factors including the FOV, resolution, type of imaging sequence, magnetic field inhomogeneity and RF inhomogeneity. Therefore, simulations were carried out to evaluate the performance of both the noiselet encoding and Fourier encoding schemes in the presence of variable levels of

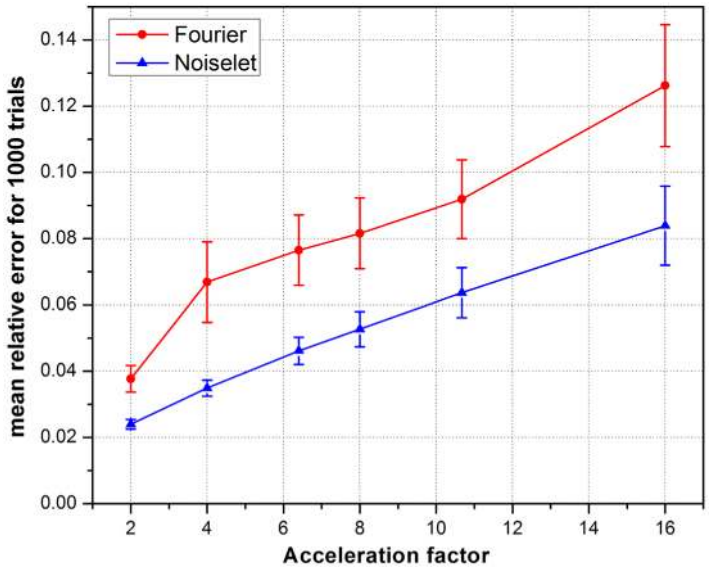

Fig 10. The mean relative error and standard deviation (vertical bar) versus the acceleration factor in MCS-MRI highlighting that noiselet encoding consistently outperforms Fourier encoding.

doi:10.1371/journal.pone.0126386.g010

noise. Different levels of random Gaussian noise were added to the measured k-space data, and MCS-MRI reconstruction was performed for noiselet and Fourier encoding schemes. For every level of noise, 1000 simulations were performed and the mean of the relative error was calculated. Fig 11 shows the mean relative error as a function of the Signal to Noise Ratio (SNR), demonstrating the comparative performance of noiselet encoding reconstructions and Fourier encoding reconstructions in the presence of noise. The plots demonstrate that noiselet encoding outperforms Fourier encoding for SNR above 20 dB for all acceleration factors, but does a poor job at extremely low SNR of 10 dB. The poor performance of noiselet encoding at 10 dB SNR can be attributed to the fact that at extremely low SNR, most of the noiselet coefficients are severely corrupted by the noise since their magnitudes are approximately uniform. In contrast, the Fourier coefficients at the center of k-space have much larger magnitudes and hence are less affected by the noise at low SNR. These large magnitude coefficients are fully utilized in reconstruction because of the centralized variable density sampling scheme, hence Fourier encoding is less affected by the noise and performs better at low SNR.

4.4 Experiments

Experiments were carried out on Siemens Skyra 3T MRI scanner with a maximum gradient strength of 40 mT/m and a maximum slew rate of 200 mT/m/sec. Informed consent was taken from healthy volunteers in accordance with the Institution's ethics policy. To validate the practical implementation of noiselet encoding, the pulse sequence shown in Fig 1 was used to acquire noiselet encoded data. An RF excitation pulse with 256 points was used. The flip angle was 10° calculated by the equal integral rule described in Section 3.1, with the SAR level checked by Siemens' RF pulse programming software IDEA to be well below the safety limit and about 5% higher than that of Fourier encoding RF pulse. We also acquired the Fourier encoded data using the spin echo (SE) sequence to compare the quality of the reconstructed

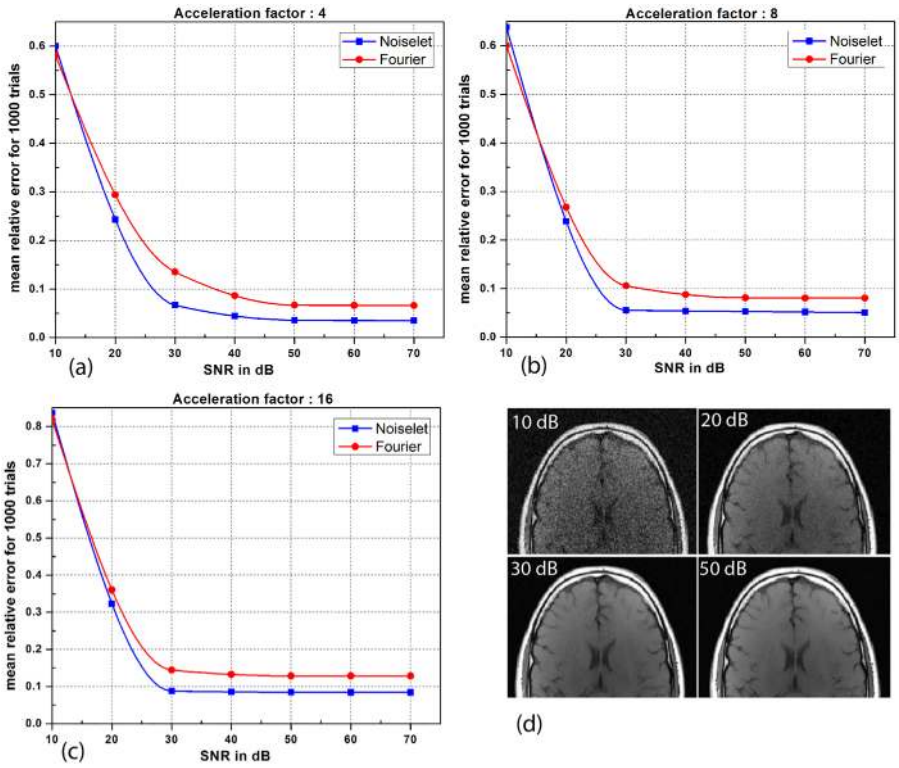

Fig 11. (a), (b) and (c): are the plots of the mean relative error as a function of the signal to noise ratio (SNR) for different number of measurements. When the SNR is greater than 20 dB, the noiselet encoding outperforms Fourier encoding in the presence of noise for all acceleration factors; **(d)**: show the brain images with SNR of 10, 20, 30 and 50 dB.

doi:10.1371/journal.pone.0126386.g011

image from the data acquired by the noiselet encoding sequence. An apodized slice selective sinc RF excitation pulse was used in the spin echo sequence with a flip angle of 10°. The protocol parameters for the noiselet encoding sequence and the Fourier encoding SE sequence were **(i) Phantom experiments** FOV = 200 mm, TE/TR = 26/750 ms, image matrix = 256 × 256; and **(ii) *In vivo* experiments** FOV = 240 mm, TE/TR = 26/750 ms, image matrix = 256 × 256.

Non-Fourier encoding in general is sensitive to field inhomogeneities, but careful design of the sequence and good shimming can result in high quality images. To reconstruct the noiselet encoded data the inverse Fourier transform was taken along the frequency encoding axis and the inverse noiselet transform was taken along the PE axis. To reconstruct the Fourier encoded data, an inverse Fourier transform was taken along both axes. Fig 12 shows the images reconstructed from the fully sampled noiselet encoded data and Fourier encoded data sets. These images demonstrate that the noiselet encoding reconstructions are practically feasible and produce artifact free images. Fig 12(c) shows a zoomed portion of the noiselet encoded image, while Fig 12(f) shows a zoomed portion of the Fourier encoded image. The zoomed images reveal that the resolution of the image from noiselet encoding with 256 noiselet excitation is the same as that of the image from Fourier encoding with 256 phase encodes. Fig 12(g) and 12(i) show the T2 weighted images for the brain with noiselet encoding and Fourier encoding, respectively. Fig 12(h) and 12(j) show the T1 weighted images for the brain with noiselet encoding and Fourier encoding, respectively. It is evident from the *in vivo* images that the proposed noiselet encoding is feasible in practice.

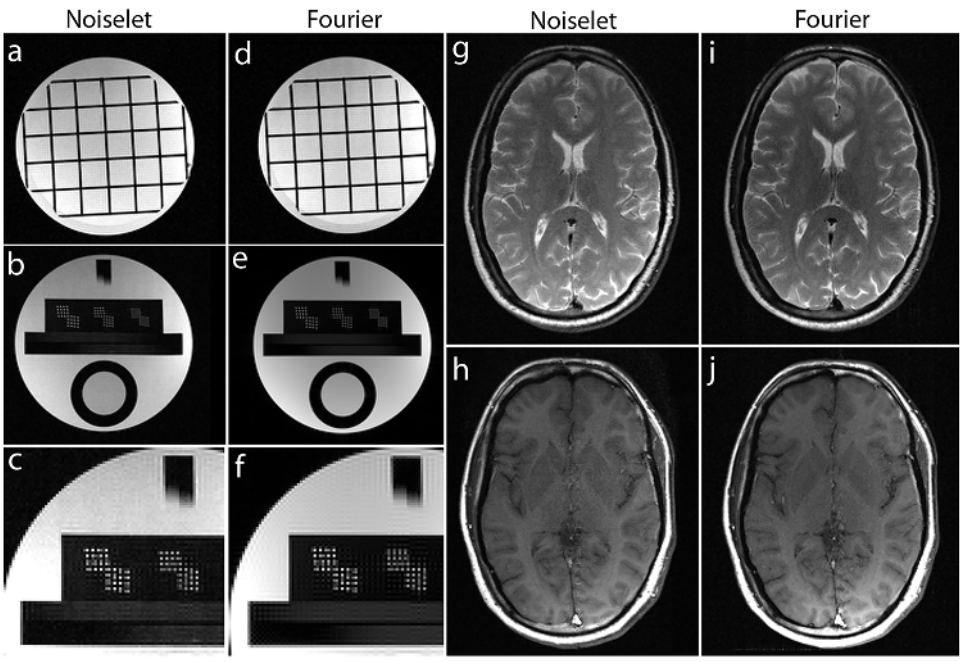

Fig 12. Images reconstructed using fully sampled noiselet encoded and Fourier encoded data acquired on the 3T scanner (up/down: phase encodes, left/right: frequency encode). The noiselet encoded data was acquired using the pulse sequence described in section III C, and Fourier encoded data was acquired using a conventional spin echo sequence. **(c)-(f)**: show the zoomed portion of the images in (b) and (e) respectively, with the zoomed images demonstrating that noiselet encoding provides similar image resolution to that of Fourier encoding; **(g)-(h)**: show T2 and T1 weighted brain images using noiselet encoding respectively; **(i)-(j)**: show T2 and T1 weighted brain images using Fourier encoding respectively. These *in vivo* images demonstrate the practical feasibility of the proposed noiselet encoding scheme.

doi:10.1371/journal.pone.0126386.g012

To validate the feasibility of the proposed reconstruction method, we performed retrospective under-sampling on the acquired noiselet encoded data and Fourier encoded data to simulate accelerated data acquisition. After retrospective under-sampling, the unconstrained optimization program (10) was solved using the non-linear conjugate gradient method to reconstruct the desired image for different acceleration factors. Fig 13(a)–13(c) shows the reconstructed images for the acceleration factors of 4, 8 and 16 on the Fourier encoded data while Fig 13(d)–13(f) shows the corresponding difference images. Similarly, Fig 13(g)–13(i) shows the reconstructed images for the acceleration factors of 4, 8 and 16 on the noiselet encoded data, and Fig 13(j)–13(l) shows the corresponding difference images for noiselet encoded MCS-MRI. These results on the acquired data are consistent with the simulation results and indicate that the noiselet encoding is superior to the Fourier encoding in preserving resolution.

Fig 13(A)–13(H) shows the zoomed portion of the reconstructed images with Fourier encoding and noiselet encoding. One can distinguish between the small dots in the zoomed images reconstructed with noiselet encoding while it is difficult to distinguish these dots in the images reconstructed with Fourier encoding. This demonstrates that noiselet encoding is able to preserve resolution better than the Fourier encoding. Fig 14 show the images reconstructed with Fourier encoding and noiselet encoding for various acceleration factors on the data acquired for one axial slice of the brain. Since the SNR of the *in vivo* images is less than in the phantom images, reconstruction is shown only up to an acceleration factor of 8. The difference images demonstrate that noiselet encoding outperforms Fourier encoding for all acceleration

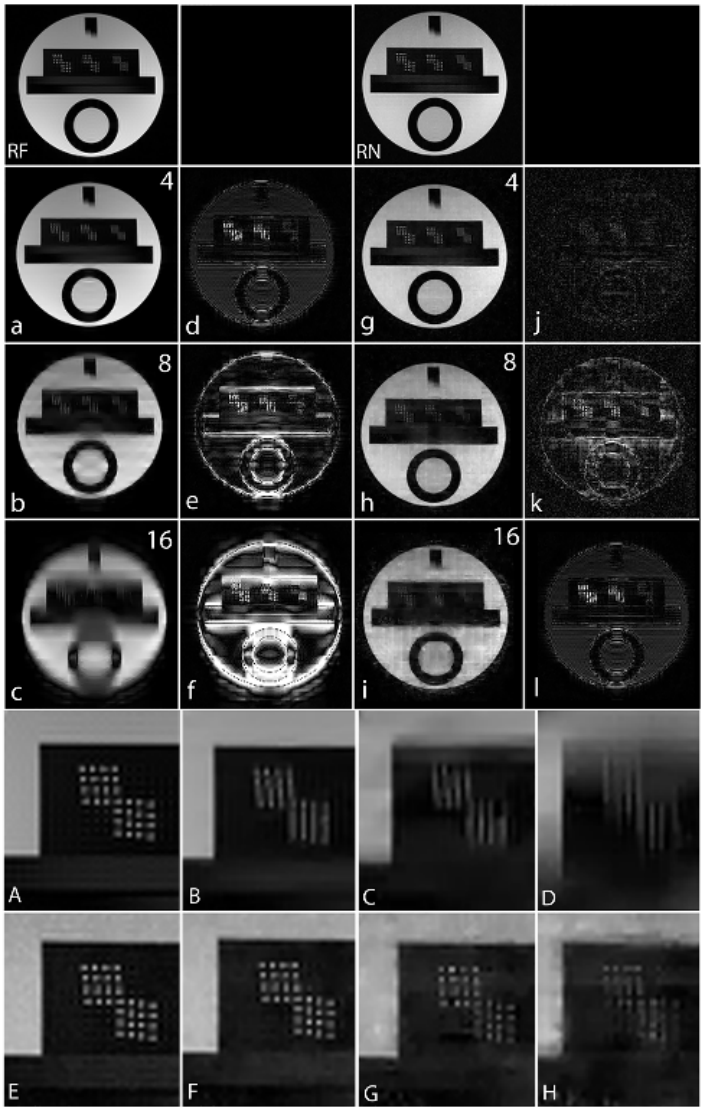

Fig 13. MCS-MRI reconstruction on the acquired noiselet encoded and Fourier encoded data for different acceleration factors (up/down: phase encodes, left/right: frequency encode). RF: shows reference image reconstructed from fully sampled Fourier encoded data; **RN**: shows reference image reconstructed from fully sampled Noiselet encoded data; **(a)-(c)**: show images reconstructed using Fourier encoding for acceleration factor of 4, 8 and 16 respectively; **(d)-(f)**: show the difference images using Fourier encoding for acceleration factor of 4, 8 and 16 respectively; **(g)-(i)**: show images reconstructed using noiselet encoding for acceleration factor of 4, 8 and 16 respectively; **(j)-(l)**: show the difference images using noiselet encoding for acceleration factor of 4, 8 and 16 respectively. The result here aligns with the simulation results and noiselet encoding outperforms Fourier encoding in preserving resolution. **(A-H)**: Zoomed portion of phantom images reconstructed with Fourier encoding and noiselet encoding with different acceleration factors. **(A)**: shows the original image reconstructed from fully sampled Fourier encoded data; **(B), (C) and (D)**: show the Fourier encoded reconstructed images for acceleration factors of 4, 8 and 16 respectively; **(E)**: shows the image reconstructed from fully sampled noiselet encoded data; **(F), (G) and (H)**: show the noiselet encoded reconstructed images for acceleration factors of 4, 8 and 16 respectively demonstrating that noiselet encoding produces improved resolution images than than Fourier encoding at all acceleration factors.

doi:10.1371/journal.pone.0126386.g013

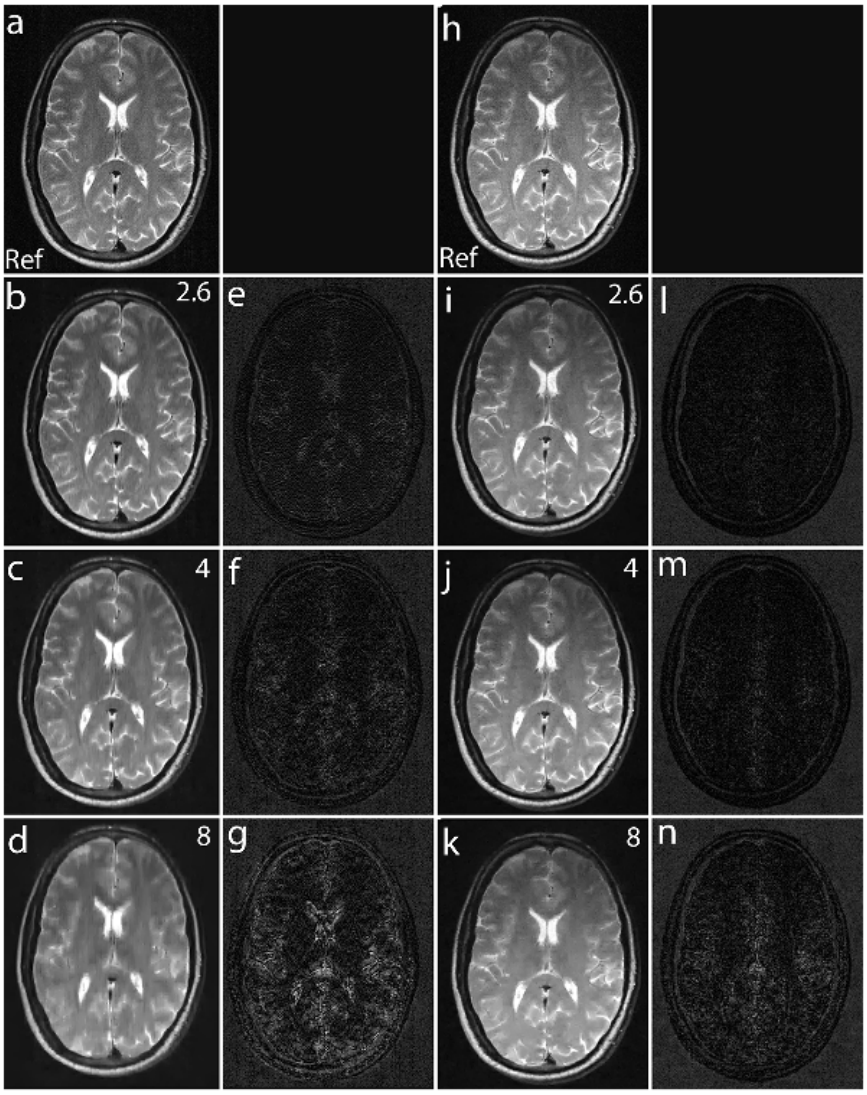

Fig 14. MCS-MRI reconstruction on *in vivo* brain images using acquired noiselet encoded and Fourier encoded data for different acceleration factors (up/down: phase encodes, left/right: frequency encode). (a): shows reference image reconstructed from fully sampled Fourier encoded data; **(b)-(d)**: show images reconstructed using Fourier encoding for acceleration factor of 2.6, 4 and 8 respectively; **(e)-(g)**: show the difference images using Fourier encoding for acceleration factor of 2.6, 4 and 8 respectively; **(h)**: shows reference image reconstructed from fully sampled Noiselet encoded data; **(i)-(k)**: show images reconstructed using noiselet encoding for acceleration factor of 2.6, 4 and 8 respectively; **(l)-(n)**: show the difference images using noiselet encoding for acceleration factor of 2.6, 4 and 8 respectively. It can be seen from the difference images that noiselet encoding outperforms Fourier encoding on the acquired invivo data. The loss in resolution is clearly visible for Fourier encoding at an acceleration factor of 8.

doi:10.1371/journal.pone.0126386.g014

factors. In particular, at the acceleration factor of 8 the image reconstructed with Fourier encoded data has significantly poorer resolution compared to the image reconstructed with noiselet encoded data.

5 Discussion

We have presented a new method of encoding the MR data in PE direction with noiselet basis functions for accelerating MRI scans using MCS-MRI reconstruction. The simulation results demonstrate that the proposed encoding gives rise to a multichannel measurement matrix with improved RIP, and the reconstruction method using the noiselet bases outperforms the conventional Fourier encoding scheme. The mean relative error for noiselet encoding at the acceleration factor of 16 is comparable to that of Fourier encoding at the acceleration factor of 8, demonstrating that higher acceleration factors can be achieved with noiselet encoding than the Fourier encoding in the MCS framework.

The reconstruction from the noiselet encoding scheme preserves image spatial resolution far better than the Fourier encoding scheme. The Fourier encoding scheme intelligently exploits the property of k-space since most of the energy is concentrated at the center of the k-space. Therefore, densely sampling the center and randomly under-sampling the outer regions of the k-space retains most of the energy in the acquired data. However retaining most of the energy does not imply that most of the information is captured in the acquisition. The low energy (high frequency) component in the outer k-space contains the information about the fine features of the image that the variable density random under-sampling pattern fails to capture. Therefore, the images reconstructed with the Fourier encoding scheme look visually good but have reduced resolution due to insufficient information about the high frequency components in the acquired data. On the other hand, noiselet encoding completely spreads out the energy of the signal in the measurement domain. Therefore each measurement in the noiselet domain has sufficient information to reconstruct the fine details of the image, thus preserving the resolution better than the Fourier encoding.

Noiselet basis functions have some interesting properties that can be exploited, for example noiselets are unitary basis functions and have complex conjugate symmetry. This conjugate symmetry property can be exploited in a way similar to that of the Fourier encoding for partial acquisition [48, 49]. Another interesting property of noiselet basis functions, as for the Fourier basis functions, is that regular under-sampling in the noiselet domain results in aliasing in the image domain. Therefore in the case of regular under-sampling in the noiselet domain, unaliasing with SENSE [8] alone can also be used for noiselet encoding.

In general the implementation of non-Fourier encoding suffers from a few limitations, and hence the current implementation of noiselet encoding also suffers from these limitations as summarized below. (i) In 2D imaging implementation of noiselet encoding, the excitation of noiselet profile is not slice selective, thus a slice selective 180° pulse is required after excitation, which limits the noiselet encoding to spin echo type sequences. The spin echo sequence always have long TR, therefore the proposed noiselet encoding can only be used for applications requiring long TR, such as structural scans, but will be of little use in dynamic imaging. (ii) In the current implementation, to simplify the design of noiselet excitation pulse we have used direct Fourier transform method that limits the excitation to the low flip angle regime, resulting in the sacrifice of some available SNR. (iii) The duration of noiselet RF excitation pulse is long compared to the conventional sinc RF pulse and the noiselet encoding can only be implemented in one direction in the current implementation. (iv) Due to dielectric effects, etc, in practice, B1 field is always not perfectly homogeneous. Because B1 is used for spatial encoding in the proposed noiselet encoding scheme, B1 inhomogeneity may introduce some

perturbations to the noiselet measurement matrix, which in turn may result in some image artifact if the perturbation is large.

The above limitations are not specific to noiselet encoding scheme but are common to all non-Fourier encoding schemes. Here we discuss some probable solutions to the above mentioned problems. (i) The problem of slice selection can be alleviated using a 3D gradient echo (GRE) sequences where a 3D volume can be excited with a noiselet profile in one dimension and other two dimensions can be Fourier encoded. (ii) The low tip angle in current implementation is the limitation of the direct Fourier transform method used to compute the RF pulse. It is not an intrinsic limitation of noiselet encoding. Although difficult, computation of large tip angle noiselet RF pulse is possible by using nonlinear computation methods such as direct iterative solution of Bloch equation [50] and the SLR method [51], which are currently being investigated. (iii) The duration of the RF pulse can be reduced by using parallel-transmit and multiple dimensional excitation of noiselet profiles to achieve encoding [50, 52]. This is our ongoing research. (iv) The perturbations to the measurement matrix induce an equivalent deterministic noise additive to the measured MR signals. When the inverse noiselet transform is applied directly to the fully sampled dataset to reconstruct the image, a structured artifact may show up if the perturbation is large. This problem can be alleviated when the CS reconstruction method as given in (10) is used for image reconstruction. This is because the CS reconstruction algorithm has inherent denoising capability, which can suppress small perturbations by enforcing the prescribed bound ϵ on the reconstruction error. Refer to Section 2.2 and the references therein for detailed discussions. For this reason and also because of the high quality of the new 3T scanner used in our experiments, we have not observed structured image artifacts in the experiments presented in Section 4.4.

6 Conclusion

In this paper we have introduced a method of acquiring data in the noiselet domain and presented a method for the design and implementation of pulse sequences to acquire data in the noiselet domain. The performance of the noiselet encoding has been thoroughly evaluated by extensive numerical analysis, simulation and experiments. The results indicate that the multichannel noiselet measurement matrix has better RIP than that of its Fourier counterpart, and that the noiselet encoding scheme in MCS-MRI outperforms the conventional Fourier encoding in preserving image resolution, and can achieve higher acceleration factors than the conventional Fourier encoding scheme. The implementation of noiselet encoding by tailoring spin echo sequence demonstrates that the proposed encoding scheme is pragmatic. The proposed technique has the potential to accelerate image acquisition in applications that require high resolution images.

As an emerging technique, the proposed noiselet encoding needs further improvements to overcome its limitations in current implementation. We are currently working on the improvements following the technical approach outlined in Discussion. It is expected that upon completion of these improvements, the proposed noiselet encoding scheme should be able to replace the conventional Fourier encoding in many CS MRI applications reported in the current literature to achieve better imaging quality and speed.

Supporting Information

S1 Matlab Code. Contains Matlab code used in the simulations and experiments of this manuscript.
(ZIP)

S1 Data. Contains data used in the simulations and experiments.
(ZIP)

Acknowledgments

The authors would like to thank the anonymous reviewers for useful comments on the manuscript that have improved the presentation.

Author Contributions

Conceived and designed the experiments: KP JZ. Performed the experiments: KP. Analyzed the data: KP JZ. Contributed reagents/materials/analysis tools: KP JZ GE. Wrote the paper: KP JZ GE.

References

1. Donoho DL. Compressed sensing. Information Theory, IEEE Transactions on. 2006; 52(4):1289–1306. doi: 10.1109/TIT.2006.871582
2. Candès EJ, Romberg J, Tao T. Robust uncertainty principles: Exact signal reconstruction from highly incomplete frequency information. Information Theory, IEEE Transactions on. 2006; 52(2):489–509. doi: 10.1109/TIT.2005.862083
3. Candes E, Romberg J. Sparsity and incoherence in compressive sampling. Inverse problems. 2007; 23 (3):969. doi: 10.1088/0266-5611/23/3/008
4. Candes EJ, Romberg JK. Signal recovery from random projections. In: Electronic Imaging 2005. International Society for Optics and Photonics; 2005. p. 76–86.
5. Candes EJ, Tao T. Near-optimal signal recovery from random projections: Universal encoding strategies. Information Theory, IEEE Transactions on. 2006; 52(12):5406–5425. doi: 10.1109/TIT.2006.885507
6. Lustig M, Donoho DL, Santos JM, Pauly JM. Compressed sensing MRI. Signal Processing Magazine, IEEE. 2008; 25(2):72–82. doi: 10.1109/MSP.2007.914728
7. Lustig M, Donoho D, Pauly JM. Sparse MRI: The application of compressed sensing for rapid MR imaging. Magnetic resonance in medicine. 2007; 58(6):1182–1195. doi: 10.1002/mrm.21391 PMID: 17969013
8. Pruessmann KP, Weiger M, Scheidegger MB, Boesiger P. SENSE: sensitivity encoding for fast MRI. Magnetic resonance in medicine. 1999; 42(5):952–962. doi: 10.1002/(SICI)1522-2594(199911)42:5%3C952::AID-MRM16%3E3.3.CO;2-J PMID: 10542355
9. Sodickson DK, Manning WJ. Simultaneous acquisition of spatial harmonics (SMASH): fast imaging with radiofrequency coil arrays. Magnetic Resonance in Medicine. 1997; 38(4):591–603. doi: 10.1002/mrm.1910380414 PMID: 9324327
10. Griswold MA, Jakob PM, Heidemann RM, Nittka M, Jellus V, Wang J, et al. Generalized autocalibrating partially parallel acquisitions (GRAPPA). Magnetic Resonance in Medicine. 2002; 47(6):1202–1210. doi: 10.1002/mrm.10171 PMID: 12111967
11. Otazo R, Sodickson D. Distributed compressed sensing for accelerated MRI. In: Proceedings of the 17th Annual Meeting of ISMRM; 2009. p. 378.
12. Liang D, Liu B, Wang J, Ying L. Accelerating SENSE using compressed sensing. Magnetic Resonance in Medicine. 2009; 62(6):1574–1584. doi: 10.1002/mrm.22161 PMID: 19785017
13. Liang D, Liu B, Ying L. Accelerating sensitivity encoding using compressed sensing. In: Engineering in Medicine and Biology Society, 2008. EMBS 2008. 30th Annual International Conference of the IEEE. IEEE; 2008. p. 1667–1670.
14. Otazo R, Kim D, Axel L, Sodickson DK. Combination of compressed sensing and parallel imaging for highly accelerated first-pass cardiac perfusion MRI. Magnetic Resonance in Medicine. 2010; 64 (3):767–776. doi: 10.1002/mrm.22463 PMID: 20535813
15. Lustig M, Pauly JM. SPIRiT: Iterative self-consistent parallel imaging reconstruction from arbitrary k-space. Magnetic Resonance in Medicine. 2010; 64(2):457–471. doi: 10.1002/mrm.22428 PMID: 20665790

16. Ji JX, Zhao C, Lang T. Compressed sensing parallel magnetic resonance imaging. In: Engineering in Medicine and Biology Society, 2008. EMBS 2008. 30th Annual International Conference of the IEEE. IEEE; 2008. p. 1671–1674.
17. Lustig M, Santos JM, Donoho DL, Pauly JM. kt SPARSE: High frame rate dynamic MRI exploiting spatio-temporal sparsity. In: Proceedings of the 13th Annual Meeting of ISMRM, Seattle; 2006. p. 2420.
18. Jung H, Sung K, Nayak KS, Kim EY, Ye JC. k-t FOCUSS: A general compressed sensing framework for high resolution dynamic MRI. Magnetic Resonance in Medicine. 2009; 61(1):103–116. doi: 10.1002/mrm.21757 PMID: 19097216
19. Qiu C, Lu W, Vaswani N. Real-time dynamic MR image reconstruction using Kalman filtered compressed sensing. In: Acoustics, Speech and Signal Processing, 2009. ICASSP 2009. IEEE International Conference on. IEEE; 2009. p. 393–396.
20. Jung H, Ye JC. Motion estimated and compensated compressed sensing dynamic magnetic resonance imaging: What we can learn from video compression techniques. International Journal of Imaging Systems and Technology. 2010; 20(2):81–98. doi: 10.1002/ima.20231
21. Candès EJ. The restricted isometry property and its implications for compressed sensing. Comptes Rendus Mathematique. 2008; 346(9):589–592.
22. Tillmann AM, Pfetsch ME. The computational complexity of the restricted isometry property, the nullspace property, and related concepts in compressed sensing. arXiv preprint arXiv:12052081. 2012;.
23. Candes EJ, Tao T. Decoding by linear programming. Information Theory, IEEE Transactions on. 2005; 51(12):4203–4215. doi: 10.1109/TIT.2005.858979
24. Bayati M, Lelarge M, Montanari A. Universality in polytope phase transitions and iterative algorithms. In: Information Theory Proceedings (ISIT), 2012 IEEE International Symposium on. IEEE; 2012. p. 1643–1647.
25. Haldar JP, Hernando D, Liang ZP. Compressed-Sensing MRI with random encoding. Medical Imaging, IEEE Transactions on. 2011; 30(4):893–903. doi: 10.1109/TMI.2010.2085084
26. Blanchard JD. Towards deterministic compressed sensing. In: Proceedings of the National Academy of Sciences,; 2013. p. 1147–1148.
27. Puy G, Marques JP, Gruetter R, Thiran J, Van De Ville D, Vandergheynst P, et al. Spread spectrum magnetic resonance imaging. Medical Imaging, IEEE Transactions on. 2012; 31(3):586–598. doi: 10.1109/TMI.2011.2173698
28. Liang D, Xu G, Wang H, King KF, Xu D, Ying L. Toeplitz random encoding MR imaging using compressed sensing. In: Biomedical Imaging: From Nano to Macro, 2009. ISBI'09. IEEE International Symposium on. IEEE; 2009. p. 270–273.
29. Sebert F, Zou Y, Ying L. Compressed Sensing MRI with random B1 field. Proc ISMRM,(Toronto, Canada, 2008). 2008;p. 3151.
30. Wang H, Liang D, King K, Ying L. Toeplitz random encoding for reduced acquisition using compressed sensing. Proc ISMRM,(Honolulu, Hawai, 2009). 2009;p. 2669.
31. Qu X, Chen Y, Zhuang X, Yan Z, Guo D, Chen Z. Spread spectrum compressed sensing MRI using chirp radio frequency pulses. arXiv preprint arXiv:13015451. 2013;.
32. Liu Z, Nutter B, Mitra S. Compressive sampling in fast wavelet-encoded MRI. In: Image Analysis and Interpretation (SSIAI), 2012 IEEE Southwest Symposium on. IEEE; 2012. p. 137–140.
33. Wang H, Liang D, King KF, Ying L. Three-dimensional hybrid-encoded MRI using compressed sensing. In: Biomedical Imaging (ISBI), 2012 9th IEEE International Symposium on. IEEE; 2012. p. 398–401.
34. Wang H, Liang D, King KF, Nagarsekar G, Ying L. Three-dimensional hybrid-encoded MRI using compressed sensing. In: International Society of Magnetic Resonance in Medicine Scientific Meeting; 2012. p. 73.
35. Coifman R, Geshwind F, Meyer Y. Noiselets. Applied and Computational Harmonic Analysis. 2001; 10 (1):27–44. doi: 10.1006/acha.2000.0313
36. Tuma T, Hurley P. On the incoherence of noiselet and Haar bases. In: SAMPTA'09; 2009. p. General–session.
37. Datta S, Ni K, Mahanti P, Roudenko S. Stability of efficient deterministic compressed sensing for images with chirps and Reed-Muller sequences. Applied Mathematics. 2013; 4:183. doi: 10.4236/am.2013.41A029
38. Ni K, Datta S, Mahanti P, Roudenko S, Cochran D. Efficient deterministic compressed sensing for images with chirps and Reed-Muller codes. SIAM Journal on Imaging Sciences. 2011; 4(3):931–953. doi: 10.1137/100808794

39. Applebaum L, Howard S, Searle S, Calderbank R. Chirp sensing codes: Deterministic compressed sensing measurements for fast recovery. Applied and Computational Harmonic Analysis. 2009; 26:283–290. doi: 10.1016/j.acha.2008.08.002

40. Elad M. Sparse and redundant representations: from theory to applications in signal and image processing. Springer; 2010.

41. Ma S, Yin W, Zhang Y, Chakraborty A. An efficient algorithm for compressed MR imaging using total variation and wavelets. In: Computer Vision and Pattern Recognition, 2008. CVPR 2008. IEEE Conference on. IEEE; 2008. p. 1–8.

42. Panych LP, Zientara GP, Jolesz FA. MR image encoding by spatially selective rf excitation: An analysis using linear response models. International journal of imaging systems and technology. 1999; 10 (2):143–150. doi: 10.1002/(SICI)1098-1098(1999)10:2%3C143::AID-IMA5%3E3.3.CO;2-N

43. Mitsouras D, Hoge WS, Rybicki FJ, Kyriakos WE, Edelman A, Zientara GP. Non-Fourier-encoded parallel MRI using multiple receiver coils. Magnetic resonance in medicine. 2004; 52(2):321–328. doi: 10.1002/mrm.20172 PMID: 15282814

44. Panych LP, Zientara GP, Saiviroonporn P, Yoo SS, Jolesz FA. Digital wavelet-encoded MRI: A new wavelet-encoding methodology. Journal of Magnetic Resonance Imaging. 1998; 8(5):1135–1144. doi: 10.1002/jmri.1880080520 PMID: 9786153

45. Panych LP, Oesterle C, Zientara GP, Hennig J. Implementation of a fast gradient-echo SVD encoding technique for dynamic imaging. Magnetic resonance in medicine. 1996; 35(4):554–562. doi: 10.1002/mrm.1910350415 PMID: 8992206

46. Nishimura DG. Principles of magnetic resonance imaging. Stanford University; 2010.

47. Kim Y, Fessler J, Noll D. Smoothing effect of sensitivity map on fMRI data using a novel regularized self-calibrated estimation method. In: Proc. Intl. Soc. Mag. Res. Med; 2008. p. 1267.

48. Margosian PM, DeMeester G, Liu H. Partial Fourier acquisition in MRI. eMagRes. 1996;.

49. McGibney G, Smith M, Nichols S, Crawley A. Quantitative evaluation of several partial Fourier reconstruction algorithms used in MRI. Magnetic resonance in medicine. 1993; 30(1):51–59. doi: 10.1002/mrm.1910300109 PMID: 8371675

50. Xu D, King KF, Zhu Y, McKinnon GC, Liang ZP. Designing multichannel, multidimensional, arbitrary flip angle RF pulses using an optimal control approach. Magnetic Resonance in Medicine. 2008; 59 (3):547–560. doi: 10.1002/mrm.21485 PMID: 18306407

51. Pauly J, Le Roux P, Nishimura D, Macovski A. Parameter relations for the Shinnar-Le Roux selective excitation pulse design algorithm. Medical Imaging, IEEE Transactions on. 1991; 10(1):53–65. doi: 10.1109/42.75611

52. Grissom WA, Xu D, Kerr AB, Fessler JA, Noll DC. Fast large-tip-angle multidimensional and parallel RF pulse design in MRI. Medical Imaging, IEEE Transactions on. 2009; 28(10):1548–1559. doi: 10.1109/TMI.2009.2020064